Available online at www.sciencedirect.com

ScienceDirect

International Journal of Heat and Fluid Flow 28 (2007) 306–317

International Journal of HEAT AND FLUID FLOW

www.elsevier.com/locate/ijhff

Heat transfer augmentation in a rectangular channel with a vee-shaped vortex generator

A. Sohankar

Mechanical Engineering Department, Faculty of Engineering, Yazd University, Yazd, Iran

Received 15 August 2005; received in revised form 9 March 2006; accepted 22 March 2006
Available online 18 May 2006

Abstract

The unsteady flow and heat transfer are simulated using LES and DNS for a channel with two angled ribs as a vee-shaped vortex generator to augment heat transfer. The vortex generators are attached on the bottom wall of the channel and their angles in respect to the main flow are between 10° and 30°. The Prandtl number is 0.71 and the Reynolds numbers based on the inflow velocity and the height of channel are from 200 to 2000. Based on the results of this work, the variations of the Nusselt number, pressure coefficient, bulk temperature, friction factor and Colburn factor with the Reynolds numbers and the incidence angles are provided.

The relation between the key parameters of the velocity (friction factor f) and thermal (Colburn factor J) boundary layers is calculated for all cases and their values are compared with the predicted values by the Chilton–Colburn analogy.

A comparison between the DNS and LES results is performed and it is found that relatively similar results are obtained from a LES simulation with fine grid and a DNS simulation with finer grid.

Thermal performance parameter, JF, is used as a measure for the amount of the heat transfer enhancement relative to the pressure drop. The JF value increases as the Reynolds number or the incidence angles increase.

The structure of the heat transfer and fluid flow are studied using the kinetic energy, pressure, velocity and temperature fluctuations.

Keywords: Heat transfer augmentation; Vortex generator; Thermal performance parameter; LES; DNS

1. Introduction

During recent years, serious attempts have been made to apply different active and passive mechanisms for heat transfer enhancement in compact heat exchangers for the automotive industry, air-conditioning and refrigerant applications, internal cooling for gas turbine blades, electrical circuits in electronic chipsets, etc. Achieving higher heat transfer rates through various augmentation techniques can result in substantial energy savings, more compact and less expensive apparatus with higher thermal efficiency. Different mechanisms such as creating electric or magnetic fields, jets, forced oscillations, fluid additives and special surface geometries, may be used for heat transfer enhancement. It can be categorized in two groups, main-flow and secondary-flow enhancement in active or passive way, see Webb (1994), and Jacobi and Shah (1995, 1998). Methods such as electric or acoustic fields, surface vibration and mechanical devices are called active because they require external power, whereas passive methods use special surface geometries or fluid additive, and do not require external power. Wavy walls, louvered and strip fins are examples of passive main-flow enhancement methods, while flow pulsation is an active main-flow method. The use of surface protuberances is a passive secondary-flow method and is based on developing boundary layers or stream-wise fluctuations, creating swirl or vortices and flow destabilization or turbulence intensification. In general, mixing the main flow, reducing the flow boundary layer, raising the turbulent intensity, creating rotating and secondary flow are the main reasons for the increase of the heat transfer. Vortex generation is a

E-mail address: asohankar@yazduni.ac.ir

0142-727X/$ - see front matter © 2006 Elsevier Inc. All rights reserved.
doi:10.1016/j.ijheatfluidflow.2006.03.002

Nomenclature

B, H, L	channel sides (see Fig. 1)
b, d, $L2$	vortex generator sides (see Fig. 1)
Cp	pressure coefficient
f	friction factor
h	convection heat transfer coefficient
k	conduction heat transfer coefficient
$L1$	distance between leading edge of vortex generator and inlet (see Fig. 1)
k_{sgs}	subgrid turbulent kinetic energy
J	Colburn factor
JF	thermal performance parameter
$Nu = hH/k$	Nusselt number
p	pressure
Pr	Prandtl number
$Re = UH/\nu$	Reynolds number
s	distance between vortex generators (see Fig. 1)
T	temperature
t	time
U	inflow velocity
u, v, w	velocity components
α	vortex generator angles (see Fig. 1)
Δt	time step
$\varDelta$	filter length
θ	non dimensional temperature
ρ	fluid density
ν	kinematic viscosity
ν_{t}	turbulent eddy viscosity
$\varGamma$	circulation

Subscripts/Superscripts

$'$	fluctuation quantities
$\sim$	grid filter quantities
$\_$	test filter quantities
*	reference quantities
sgs	subgrid quantities
w	wall
in	inlet
b	bulk

promising technique for heat transfer augmentation. In recent years, vortex generators such as fins, ribs, wings, etc. have been successfully used for enhancement of heat transfer of modern thermal systems. Vortex generators generate secondary flow by swirl and destabilize the flow. Different types of vortex generators such as rectangular and triangular wings and winglets have been considered for heat transfer enhancement by Fiebig and co-workers and other researchers. For example, the effect of the streamwise vortices due to the delta vortex generators on the frost growth rate in developing laminar channel flow was experimentally investigated by Storey and Jacobi (1999). Their study demonstrated that the local frost growth rates were increased about 7% in the region where the streamwise vortices induced a surface-normal flow toward the frost surface. Chen et al. (2000) employed punched longitudinal vortex generators in the form of winglets in staggered arrangements to enhance heat transfer in finned oval-tube heat exchangers. Their numerical study showed that the ratio of heat transfer enhancement to flow loss penalty was greater than one ($Re = 300$). Liou et al. (2000) employed 12 different shaped vortex generators to study experimentally heat transfer enhancement in a sharp two-pass square channel. They found that the direction and strength of the secondary flow with respect to the heat transfer at the wall were most important fluid dynamic factors affecting the heat transfer promotion. Three-dimensional unsteady flow and heat transfer in a channel with inclined block shaped vortex generators mounted on one side of a channel flow were investigated by Sohankar and Davidson (2001). In this work, the effect of the computational domain, incidence angle, vortex generator size, discretization scheme and Reynolds number on the results was investigated. It was also reported that the flow becomes unsteady for Reynolds number larger than 1000. Gentry and Jacobi (2002) used delta wings placed at the leading edge of a flat plate to generate streamwise vortices. They reported that the local heat transfer coefficient increases as much as 300% in regions, where a vortex induces a surface normal inflow. They also found that the vortex strength increases with Reynolds number, wing aspect ratio, and wing attack angle. Numerical and experimental analyses were carried out by Leu et al. (2004) to study the heat transfer and flow in the plate fin and tube heat exchangers with inclined block shape vortex generators mounted behind the tubes ($Re = 400$–3000, $\alpha = 30°, 45°, 60°$). They reported that the case of $\alpha = 45°$ provides the best heat transfer enhancement.

The present work concentrates on the study of the unsteady heat transfer and fluid flow in a three-dimensional channel with a pair of angled ribs as a vee-shaped vortex generator ($\alpha = 10$–$30°$) for $Re = 200$–2000 and $Pr = 0.71$. This study has been made to expand the previous works of Sohankar and Davidson (2001) and Sohankar (2004) for a larger range of Reynolds numbers, using finer grids. The study of fluctuations and turbulent stresses is also made for a higher Reynolds number. A comparison between the DNS and LES results is also performed.

The organization of this paper is as follows. Section 2 is devoted to the description the flow configuration, computational domain, grid and the boundary conditions. A short review on the governing equation for DNS and LES formulation is given in Section 3. The sub-grid scale model used in this work is presented in Section 4. The analysis of the global, time-averaged and instantaneous results is presented in Section 5. Finally, some conclusions are drawn in Section 6.

2. Geometry and computational details

The physical problem considered in this study is a three-dimensional channel flow (e.g. a part of a plate fin compact heat exchanger). Two three-dimensional angled ribs as a vee-shaped vortex generator are mounted on the floor of this channel to enhance heat transfer. The computational domain and grid for the ribbed channel are shown in Fig. 1. As seen, flow is described in a coordinate system (x, y, z) in which the x-axis is aligned with the inflow, stream-wise direction, the z-axis is in the span-wise direction and the y-axis is perpendicular to both the x and $z$axes. The vee-shaped vortex generator is attached on the bottom wall of the channel and their angle in respect to the main flow is denoted by α. The sides of this vortex generator in the xz plane are denoted by $L2$ and b and the height of the vortex generator in the y direction is d. The sides of the channel are denoted L, H and B in the x, y, z directions, respectively.

All geometrical lengths are scaled with H, the channel height. Velocities are scaled with U, the inflow velocity, and physical time with H/U. In this work, (H, L, B) are set to (1, 6, 5) and $(L1, L2, S, b, d, \alpha)$ are set to 2, 2, 1, 0.2, 0.5 and 10–30°, respectively. The dimensionless temperature is defined as $\theta = (T - T_{\text{in}})/(T_{\text{W}} - T_{\text{in}})$, where T_{W} is a constant temperature at the channel walls and ribs, and T_{in} is a constant inflow temperature. The pressure scales with ρU^2, where ρ is the flow density. The Reynolds number is defined as $Re = UH/\upsilon$. The local Nusselt numbers are calculated with local temperature gradients at the wall as $Nu(x,z) = \frac{h(x,z)H}{k} = -\frac{\partial\theta}{\partial n}|_{\text{wall}}$, where $h(x, z)$ and k are the local convection heat transfer and conduction coefficients.

The time-marching calculations started with the fluid at rest, and a constant dimensionless time step, $\Delta t = 0.01$ was used. The grid distribution was non-uniform body-fitted in the xz planes. The distance from the vortex generator surface to the nearest grid point was set about 0.01 for all calculations in this study. The hyperbolic tangent was employed as a stretching function, see Fig. 1. A uniform grid between nodes was used in the y direction. In the present study, two resolutions of $122 * 34 * 98$ and $162 * 50 * 146$ grid points in the (x, y, z) directions were used. The finer resolution was employed only for DNS simulations. Due to variation of grid spacing and velocity, the local Courant number varies in the computational domain and its maximum value is about 1.66 for LES simulation.

The following boundary conditions were used. A uniform flow $(u = U,\ v = w = \theta = 0)$ was prescribed at the inlet. At the outlet, the convective boundary condition $(\frac{\partial u}{\partial \tau} + U\frac{\partial u}{\partial x} = 0)$ was used for streamwise velocity component. The Neumann condition was used for v, w and θ at the outlet. The no-slip condition was prescribed at the vortex generator surfaces, the lower $(y = 0)$ and on the upper $(y = H)$ channel walls. θ was set to one on the vortex generators and the channel walls, where $T = T_{\text{w}}$. Symmetry conditions $(\frac{\partial u}{\partial z} = \frac{\partial v}{\partial z} = \frac{\partial \theta}{\partial z} = w = 0)$ were used in the spanwise direction.

3. Governing equations

The continuity, momentum and energy equations in the dimensionless form for incompressible flow with constant fluid properties are:

$$u_{i,i} = 0 \tag{1}$$

$$\partial_t u_i + (u_i u_j)_{,j} + p_{,i} = Re^{-1} u_{i,jj} \tag{2}$$

$$\partial_t \theta + (\theta u_j)_{,j} = (RePr)^{-1} \theta_{,jj} \tag{3}$$

In the DNS simulations, the above equations were discretized and solved with an incompressible finite volume code, based on a fractional step technique with a non-staggered grid arrangement and a multi-grid pressure solver (Sohankar and Davidson, 2001). The scheme was implicit in time, and a second order Crank–Nicolson time-stepping was used. All terms were discretized using the second-order central differencing scheme.

The LES governing equations are solved using a general spatial filtering of the instantaneous equations, e.g. a box filter, to limit the range of scales in the flow field. In this

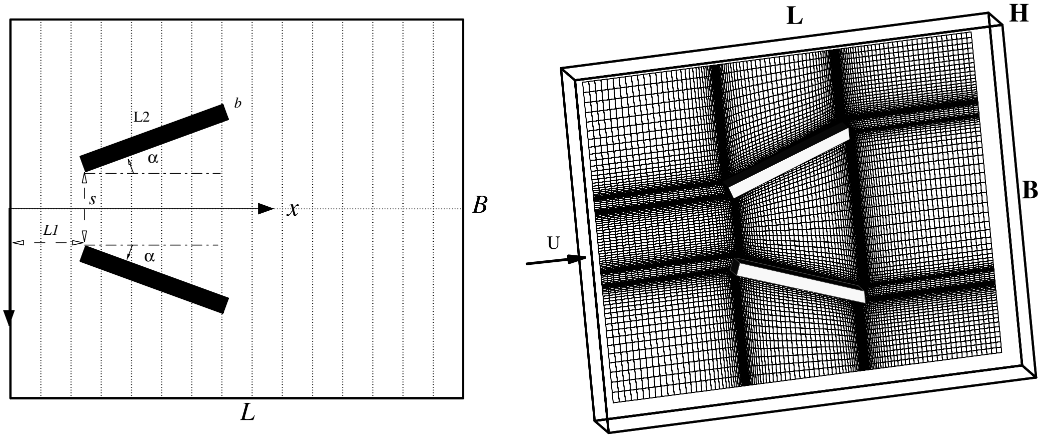

Fig. 1. Computational domain and grid on the bottom wall.

procedure, a general variable is decomposed into a large scale and a sub-grid-scale component, e.g. $f = \tilde{f} + f^{\mathrm{sgs}}$. In LES, all scales larger than a selected size (e.g. grid size) are computed exactly. Since the small scales tend to be more dissipative, isotropic, short-lived, homogeneous, random, and less affected by the boundary conditions than the larger ones, they are not explicitly simulated. For an incompressible flow of a Newtonian fluid, the filtered Navier–Stokes equations take the following form:

$$\tilde{u}_{i,i} = 0 \tag{4}$$

$$\partial_t \tilde{u}_i + (\tilde{u}_i \tilde{u}_j)_{,j} + \tilde{p}_{,i} + \tau_{ij,j} = Re^{-1} \tilde{u}_{i,jj} \tag{5}$$

The influence of the small scales on the large (resolved) scales takes place through the sub-grid-scale stresses (SGS), $\tau_{ij} = \tilde{\sigma}_{ij} - \tilde{u}_i \tilde{u}_j \quad (\sigma_{ij} = u_i u_j)$, which must be modelled with a sub-grid model. With a correctly chosen grid the sub-grid stresses in LES are only a fraction of the total stresses, thus, it is expected that the modelling error should not affect the overall accuracy of the results as much as in it in a RANS approach.

An incompressible 3D finite volume code with a collocated grid arrangement was used for solving the energy and the filtered Navier–Stokes equations. These equations were discretized and solved with an implicit fractional two-step method. Convective, viscous and sub-grid fluxes are approximated by central differences of second-order accuracy. All terms in the equations are advanced in time using the Crank–Nicolson scheme. The equations (both LES and DNS) were solved with the Gauss–Seidel scheme, whereas a multi-grid V-cycle was used to accelerate convergence, when solving the pressure equation. It is important to mention that all simulations (LES and DNS) were performed with the same computational code. Although no explicit dissipation is added to prevent the odd–even decoupling in non-staggered grid arrangement, an implicit dissipation is present. This is performed by adding the difference between the pressure gradient at the face and the node. It can be shown that this term is proportional to the third derivative of pressure (Davidson, 2001). This term corresponds to Rhie and Chow dissipation.

4. Sub-grid modelling

The success of LES depends on how accurately the SGS stresses are modelled. The most widely used SGS model is the Smagorinsky model. In this model, the proportionality factor in the SGS stresses is a constant value that must be specified prior to a simulation. The weak point in this model is that it is not suitable to use a constant that is not really a single universal constant. Also, this model is absolutely dissipative and cannot account for backscatter.

Dynamic models, which are capable of removing some of the drawbacks of the Smagorinsky model, are a suitable alternative. The first attempt to introduce a dynamic SGS eddy viscosity model was developed by Germano et al. (1991). One of the drawbacks of the dynamic model is the numerical instability associated with the negative values and the large variation of the proportionality factor, C. To avoid numerical instability owing to an extensive variation of C in time and space, spatial averaging in the homogeneous direction and additional local averaging are performed on C. This model sometimes is called the *Standard Dynamic Model.*

In the present study, a one-equation dynamic sub-grid model is employed. This model is able to capture the backscattering phenomena and is insensitive to the existence of homogeneous directions and also more stable than the standard dynamic model, see Sohankar (1998), Sohankar et al. (2000). This model was developed by Davidson (1997) and has been successfully applied to different flow configurations, see Sohankar et al. (1999, 2000), Krajnovic and Davidson (2002) and Schmidt and Thiele (2002). In this model, the eddy viscosity ($\nu_t = C^K \tilde{\varDelta} k_{\mathrm{sgs}}^{0.5}$) is based on a length scale ($l \propto \tilde{\varDelta} = (\delta V)^{1/3}$) and a velocity scale ($q^{\mathrm{sgs}} \propto \sqrt{k_{\mathrm{sgs}}}$). k_{sgs} is the sub-grid turbulent kinetic energy and it is determined by its modelled transport equation as:

$$\begin{aligned}\partial_t k_{\mathrm{sgs}} + (\tilde{u}_j k_{\mathrm{sgs}})_{,j} &= [(\nu + C^k_{\mathrm{hom}} k_{\mathrm{sgs}}^{0.5} \tilde{\varDelta}) k_{\mathrm{sgs},j}]_{,j} \\ &\quad + P_{K\mathrm{sgs}} - C^k_* k_{\mathrm{sgs}}^{1.5} / \tilde{\varDelta},\end{aligned} \tag{6}$$

$$\begin{aligned}&P_{K\mathrm{sgs}} = -\tau^a_{ij} \tilde{u}_{i,j}, \\ &\tau^a_{ij} = \tau_{ij} - \delta_{ij}\tau_{kk}/3 = -2\nu_t \tilde{S}_{ij} = -2\tilde{\varDelta} C^k k_{\mathrm{sgs}}^{0.5} \tilde{S}_{ij}, \\ &\tilde{S}_{ij} = 0.5(\tilde{u}_{i,j} + \tilde{u}_{j,i}).\end{aligned} \tag{7}$$

In $P_{K\mathrm{sgs}}$, the dynamic coefficient C^k is computed in a way similar to that used in the standard dynamic model (Germano et al., 1991; Sohankar, 1998), i.e.

$$\begin{aligned}&C^k = \frac{\ell_{ij} M_{ij}}{2 M_{ij} M_{ij}}, \quad \ell_{ij} = \overline{(\tilde{u}_i \tilde{u}_j)} - \bar{\tilde{u}}_i \bar{\tilde{u}}_j, \\ &K = \bar{k}_{\mathrm{sgs}} + 0.5\ell_{ii}, \quad M_{ij} = -\bar{\varDelta} K^{0.5} \bar{\tilde{S}}_{ij} + \tilde{\varDelta} \overline{k_{\mathrm{sgs}}^{0.5} \tilde{S}_{ij}},\end{aligned} \tag{8}$$

where ℓ_{ij} denotes the dynamic Leonard stresses. $K \equiv 0.5 T_{ii}$ and T_{ij} are the sub-grid kinetic energy and stresses on the test level, respectively (test filter operation denoted with an overbar in the relations). $\tilde{S}_{ij}$ is the strain rate tensor on the grid level.

The Smagorinsky model is based on the assumption of local equilibrium of SGS turbulent energy, i.e. $P_{k\mathrm{sgs}} - \varepsilon_{k\mathrm{sgs}} = 0$, where $\varepsilon_{k\mathrm{sgs}}$ is the dissipation of k_{sgs}. A slightly better assumption for estimating the coefficient C^k_* (in the dissipation term) would be to assume that the filtered right-hand side of the k_{sgs} equation is equal to that of the K equation, i.e.,

$$\begin{aligned}\overline{P}_{K\mathrm{sgs}} - \overline{C^k_* (k_{\mathrm{sgs}}^{1.5} / \tilde{\Delta})} &= P_K - C^k_* (K^{1.5} / \bar{\Delta}) \Rightarrow (C^k_*)^{n+1} \\ &= [P_K - \overline{P}_{K\mathrm{sgs}} + \overline{(C^k_*)^n (k_{\mathrm{sgs}}^{1.5} / \tilde{\Delta})}](\bar{\Delta} / K^{1.5})\end{aligned} \tag{9}$$

where $P_K = 2C^k \bar{\Delta} K^{0.5} \bar{\tilde{S}}_{ij} \bar{\tilde{S}}_{ij}$. The above relation gives the coefficient C^k_* in the dissipation term for time step $n+1$. Note that $(C^k_*)^n$ in Eq. (9) has been kept inside the filtering process. The dissipation cannot be negative, which requires

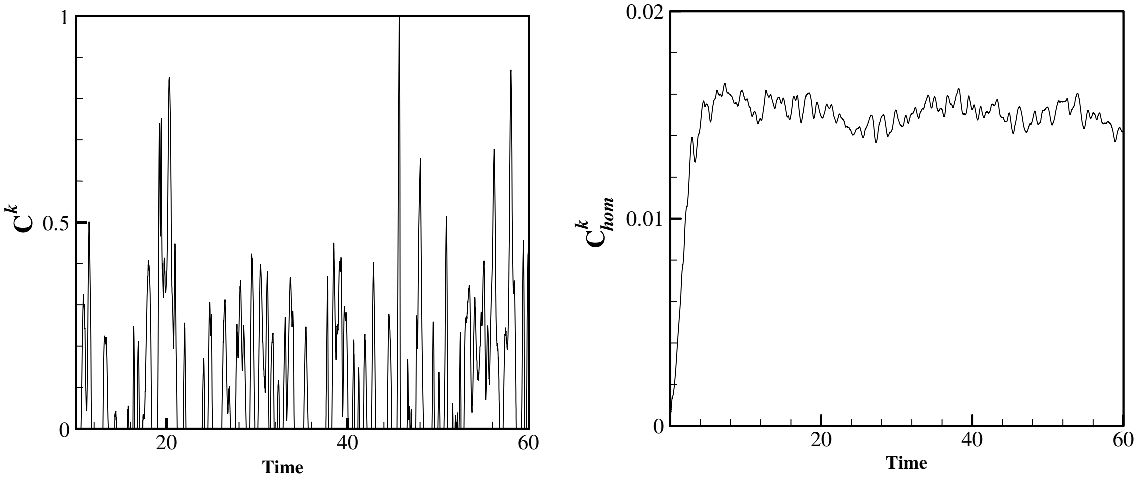

Fig. 2. Left: Time history of C^k_* (Eq. (9)) at a chosen point in calculation domain, Right: homogeneous coefficient, $C^k_{\mathrm{hom}}(t)$ (Eq. (10)), $Re = 2000$, LES.

that we limit C^k_* to positive values, i.e. $C^k_* \geqslant 0$. To ensure numerical stability, a homogenous value of C^k in space (C^K_{hom}) is used in the momentum equations and in the diffusion term in Eq. (6). The reason is that the local coefficient C^k yields a highly oscillating eddy viscosity field including a significant partition with negative values, which is destabilizing in numerical simulations, see Sohankar (1998) and Sohankar et al. (2000). C^K_{hom} is determined at each time step with the requirement that the sub-grid production of the resolved kinetic energy in the whole of the computational domain remains the same, i.e.

$$\langle 2C^k(x,y,z,t)k_{\mathrm{sgs}}^{\frac{1}{2}}\tilde{S}_{ij}\tilde{S}_{ij}\tilde{\Delta}\rangle_{xyz} = 2C^k_{\mathrm{hom}}(t)\langle k_{\mathrm{sgs}}^{\frac{1}{2}}\tilde{S}_{ij}\tilde{S}_{ij}\tilde{\Delta}\rangle_{xyz} \qquad (10)$$

where $\langle\,\rangle_{xyz}$ denotes the space averaging over the entire domain.

The idea is to include all local dynamic information through the source terms of the transport equation for k_{sgs}. This is probably physically more sound since large local variations in the dynamic coefficients appear only in the source term, and the effect of the large fluctuations in the dynamic coefficients will be smoothed out. In this way, it turns out that the need to average or limit the dynamic coefficients C^k in Eq. (8) and $(C^k_*)^{n+1}$ in Eq. (9) is eliminated altogether, see also Fig. 2. In the one-equation model, the coefficients affect the stresses in only an indirect way, while in the standard dynamics model, the C coefficient is linearly proportional to the stresses, which can make it numerically unstable.

5. Results and discussion

The effectiveness of a vee-shaped vortex generator is numerically evaluated by LES and DNS simulations. It is important to mention that the fluid flow and heat transfer become unsteady for Reynolds numbers larger than 1000. This point was also reported by Sohankar and Davidson (2001).

In Fig. 2, the time history of the dynamic coefficient in the dissipation term (C^k_* in Eq. (9)) is shown for LES simulation ($Re = 2000$) at a chosen point. As seen, C^k_* is positive and never becomes larger than one. As mentioned in Section 4, the dissipation cannot be negative, which requires that we limit C^k_* to positive values, i.e. $C^k_* \geqslant 0$. This study and also the previous work of the author (Sohankar et al., 2000) show that the dynamic coefficient C^k (Eq. (8)) can become positive or negative. The negative C^k express that this subgrid model is able to capture the backscattering phenomena. The homogeneous coefficient in space (C^k_{hom} in Eq. (10)) is also shown in Fig. 2. As seen the variation range of C^k_{hom} with time is between about 0.014 and 0.016 with a time-averaged value of about 0.015. The time-averaged values of C^k_{hom} are different for various configurations and Reynolds numbers. For example, this value for flow over a bluff body at $Re = 22\,000$ was reported to be 0.085 (Sohankar et al., 2000). Due to relatively small variation of this coefficient, no sign of numerical problems was observed here as reported by Sohankar (1998) for the standard dynamic model.

The streamwise variations of the time-averaged pressure coefficient and the bulk temperature are shown for Reynolds number from 200 to 2000 ($\alpha = 20°$) and the incidence angle 10–30° ($Re = 400$) in Fig. 3. These quantities are defined as:

$$Cp(x) = \frac{1}{A}\int\int\{(P(0) - P(x))/\rho U^2\}\mathrm{d}z\,\mathrm{d}y, \qquad (11)$$

$$\Delta\theta_b(x) = \theta_b(x) - \theta_b(0),$$

$$\theta_b(x) = \frac{\int\int \theta(x,y,z)u(x,y,z)\mathrm{d}y\,\mathrm{d}z}{\int\int u(x,y,z)\mathrm{d}y\,\mathrm{d}z}. \qquad (12)$$

The pressure decreases in the streamwise direction and this trend is similar for different Reynolds numbers and incidence angle, see Fig. 3. In the region where the vortex generator is present (approximately between $x = 2$ and $x = 4$), the pressure reduction is larger than upstream or downstream of the vortex generators. By increasing the incidence angle from 10° to 30° for a chosen Reynolds number, the pressure drop becomes larger for $x > 2$, while it is nearly

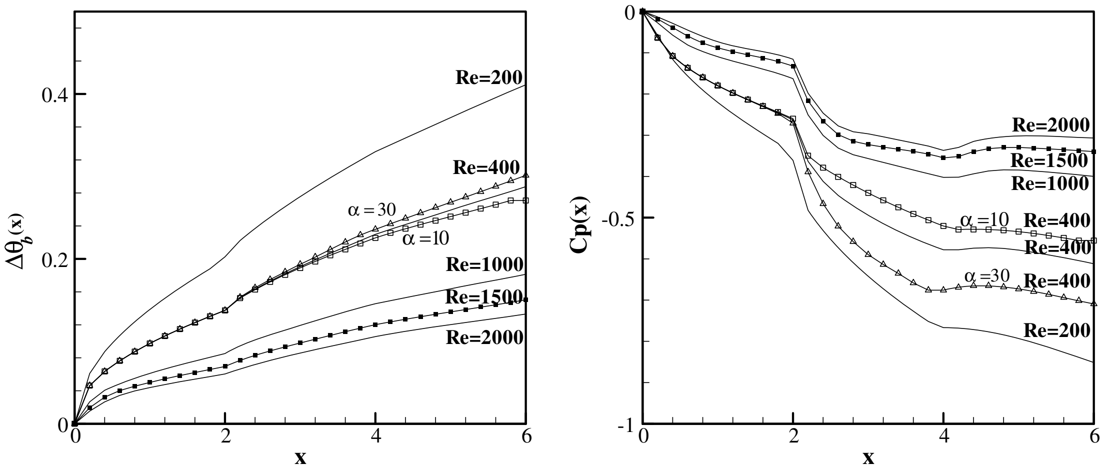

Fig. 3. Streamwise variation of the time-averaged pressure coefficient (right) and bulk temperature (left) for different Reynolds numbers and incidence angles.

identical upstream of the vortex generator. As seen from Fig. 3(right), the bulk temperature increases in the streamwise direction. However there are variations with various Reynolds numbers and incidence angles.

From the results of the present study, it is observed that, due to pressure difference between two sides of the vortex generator leg, longitudinal vortices are generated along two legs of vortex generator. These vortices detach from the vortex generator and form counter-rotating vortex pairs downstream of the vortex generator. These vortices create a down-wash movement toward the centre part of the channel between the vortex generators and also an up-wash movement away from the lower hot wall in the region outside of the vortex generators. These down-wash and up-wash flows increase the mixing of the cold fluid in the middle of the channel with the hot fluid adjacent to the channel walls; it enhances heat transfer. There are strong interactions between the longitudinal vortices and the boundary layer on the walls of the channel, especially the lower wall. These interactions affect the structure of the velocity or the thermal boundary layer by thinning it in the down-wash region and thickening it in the up-wash region on the lower wall, while the opposite trend occurs on the upper wall. In addition to generation of the longitudinal vortices, horseshoe vortices also form at the junction of the lower wall and windward face of the vortex generators. These vortices deflect downstream along both sides of the vortex generators.

The strength of the vortices changes as they develop downstream. This point is clearly seen from Fig. 4, where the variation of the time-averaged circulation in the streamwise direction, $\Gamma(x) = \int \omega_x \mathrm{d}y\,\mathrm{d}z$, is shown for $Re = 200$ and 2000 (Left: $-B/2 \leqslant z \leqslant 0$ and Right: $0 \leqslant z \leqslant B/2$). The circulation is zero at the inlet ($x = 0$), where the flow is uniform. It starts to change upstream of the vortex generators. As mentioned, the longitudinal vortices are generated at the leading edge of the vortex generators, and then they become stronger in the streamwise direction, where the vortex generators are present. This corresponds to an increase in the magnitude of the

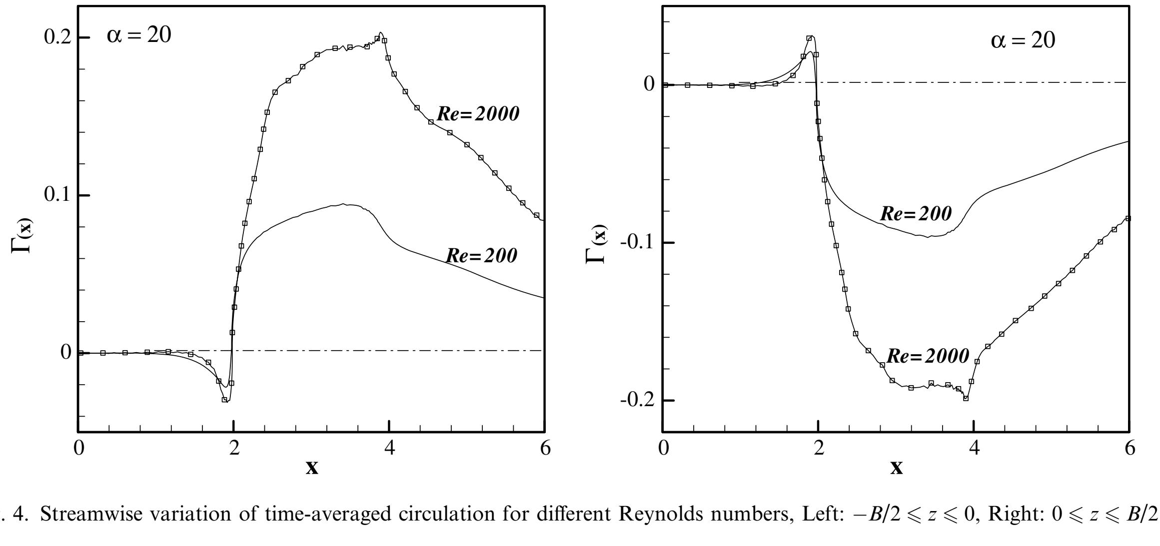

Fig. 4. Streamwise variation of time-averaged circulation for different Reynolds numbers, Left: $-B/2 \leqslant z \leqslant 0$, Right: $0 \leqslant z \leqslant B/2$.

circulation up to about $x \approx 4$, where it reaches to a peak value at the trailing edge of the vortex generators. The circulation decreases behind the vortex generators due to the reduction of the strength of the longitudinal vortices in the downstream region, where there are strong interactions between the longitudinal vortices and the boundary layer on the channel walls.

The time- and spanwise-averaged Nusselt numbers, $Nu(x) = (\int Nu(x,z)\mathrm{d}z)/\int \mathrm{d}z$, in the streamwise direction are shown on the channel walls for different Reynolds numbers in Fig. 5. As seen, $Nu(x)$ increases with increasing Reynolds numbers from 200 to 2000. A peak value in $Nu(x)$ occurs on the lower wall upstream of the vortex generators, where the horseshoe vortices form. After this peak value and along the vortex generators, the level of $Nu(x)$ gradually changes and reaches a new peak value, where the longitudinal vortices detach from the trailing edge of the vortex generators.

Fig. 6 presents the time- and area-averaged Nusselt Number, Nu, and the Colburn factor, $J = Nu/(RePr^{1/3})$, for various Reynolds numbers and incidence angles. It is important to note that Nu was averaged over two channel walls and the vortex generators. As seen, Nu and J increase by increasing the angle of incidence from 10° to 30°. It is also observed from Fig. 6 that increasing the Reynolds number increases Nu and decreases J. There is a relation between the Colburn factor, J, and the bulk temperature, $\Delta\theta_b$. An energy balance may be applied to determine this relation. If one employs an energy balance to a control volume from the inlet to an arbitrary position in the streamwise direction, i.e. $\rho A_f U(T_b(x) - T_{bin})\lambda_P = h(x)A(x)(T_w - T_{bin})$, and after a number of algebraic manipulations, the result is as: $\Delta\theta_b(x) = J(x)Pr^{-2/3}A(x)/A_f$, where λ_P, A_f and A are the specific heat at constant pressure, the cross-sectional area and the total surface area, respectively. Based on this expression, a direct relation between $J(x)$ and $\Delta\theta_b(x)$

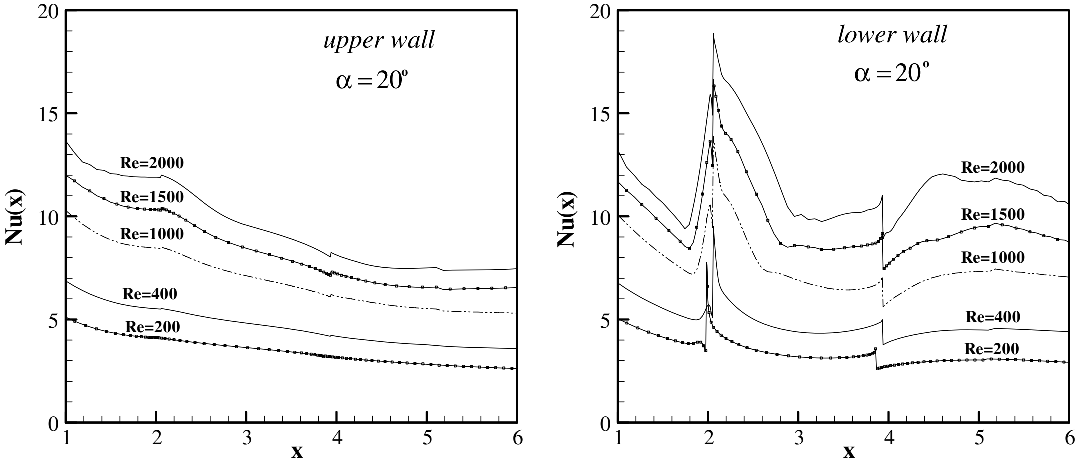

Fig. 5. Streamwise variation of time- and spanwise-averaged Nusselt number for different Reynolds numbers.

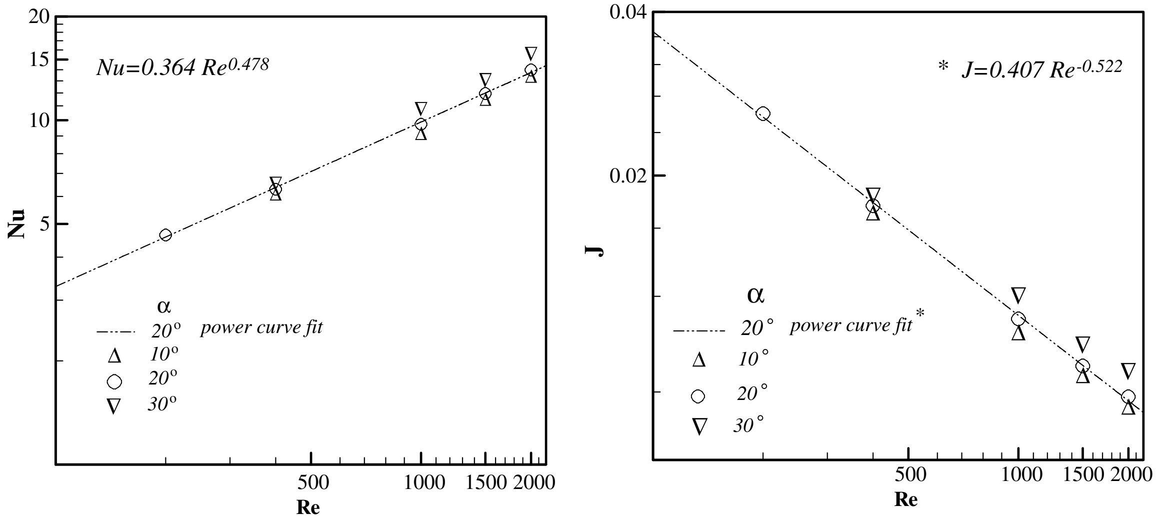

Fig. 6. Variation of time- and area-averaged Nusselt number (left) and Colburn factor (right) with Reynolds number for different incident angles.

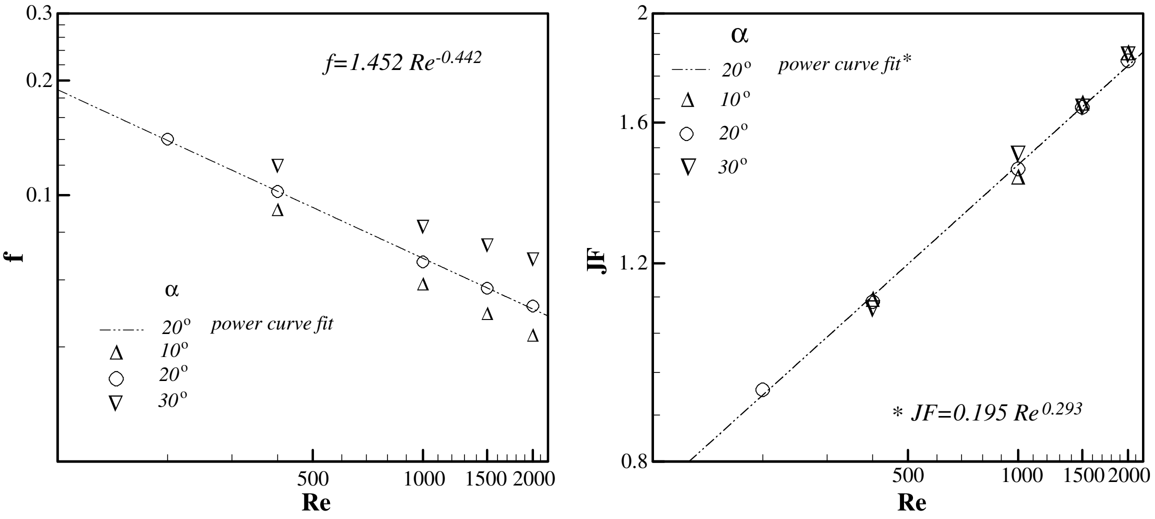

Fig. 7. Variation of time-averaged friction factor (left) and performance parameter, JF (right) with Reynolds number for different incident angles.

is observed. Thus, $J(x)$ and $\Delta\theta_b(x)$ should vary with the Reynolds number in the same way, see Figs. 3(left) and 6(right).

The variation of the time-averaged friction factor ($f = \Delta P A_f/(0.5\rho U^2 A)$) is shown in Fig. 7. It is clearly seen from this figure that f increases as the Reynolds number and incidence angle increase, see also Fig. 3(Right).

The Chilton–Colburn analogy for heat transfer relates the key parameters of the velocity (f) and thermal (J) boundary layers and it is predicted that $f/J = 8$. However, there are some restrictions associated with using this result in all cases, especially in the cases of non-zero pressure gradient. Based on the results of the present study for all cases, the ratio of f/J is calculated approximately as: 5.37 ($Re = 400$, $\alpha = 10°$), 5.7 ± 0.02 ($Re = 1000$–2000, $\alpha = 10°$), 5.55 ± 0.55 ($Re = 200$–2000, $\alpha = 20°$), 7.1 ± 0.6 ($Re = 400$–2000, $\alpha = 30°$). Thus, this ratio, f/J, depends on the Reynolds number and incidence angle and differs from the prediction of the Chilton–Colburn analogy.

In general, heat transfer enhancement in a ribbed channel in comparison to a smooth one (without vortex generator) is usually accompanied with an increase in pressure drop and requires more power. Thus, the ideal thermal-hydraulic performance evaluation of a passive augmentation method has been based on the heat enhancement for an equal pumping power ($Po = Po^*$). This means that the heat transfer coefficient, h, (or the Colburn factor, J) should become larger and the pressure drop, Δp, (or friction factor f) does not increase very much for a selected Reynolds number. A direct comparison on the basis of h (or J) and Δp (or f) is not sufficient in choosing the optimum thermal system such as a heat exchanger. This is because when h becomes larger, Δp becomes larger too. To compare the thermal and dynamic performance of a thermal system, there are constraints and criteria for heat-transfer performance comparison, for example, the identical mass-flow-rate constraint, the identical pumping power constraint, and the identical pressure drop constraint. A thermal performance parameter, $\mathrm{JF} = (h/h^*)/(Po/Po^*)^{1/3} = (J/J^*)/(f/f^*)^{1/3}$, has been used by researchers as a measure of the amount of heat transfer enhancement relative to the pressure drop for comparing heat exchanger with (J,f) and without (J^*,f^*) augmentation device (Mahmood et al., 2003). A thermal system for the same surface area and pumping power has better characteristics for heat transfer augmentation, when there is a larger value for the performance parameter, $\mathrm{JF} > 1$. In this work, the reference values (J^*,f^*) were employed from fully developed channel flow, where $Nu^* = 3.77$ and $f^* = 12/Re$.

Fig. 7(right) shows the magnitude of the performance parameter, JF, as a function of the Reynolds number. The JF value increases as the Reynolds number increases and they are greater than unity for all cases except for $Re = 200$ ($\mathrm{JF} = 0.93$). This result does not mean that the vortex generator cannot enhance heat transfer for $Re = 200$, but the resultant pressure drop is higher. This is displayed in Figs. 6(left) and 7(left), where $Nu = 4.8$ or $Nu/Nu^* = 1.23$, while $(f/f^*)^{1/3} = 1.33$. It is worth mentioning that when the reference values (J^*,f^*) were employed from the developing channel flow results instead of the developed one, the magnitude of the performance parameter is higher. In this case the correlation of the JF values for $\alpha = 20°$ is as: $\mathrm{JF} = 0.344Re^{0.25}$, where $\mathrm{JF} > 1$ for all selected Reynolds numbers between 200 and 2000.

It is found that there is a lower enhancement for the lower Reynolds numbers ($Re < 1000$) than for the higher ones. This behaviour could be explained by the following reasons. Firstly, the vortex strength at the lower Reynolds numbers is weaker than those at the higher Reynolds numbers, see Fig. 4. Secondly, an unsteady behaviour occurs for the higher Reynolds, i.e. $Re \geqslant 1000$ (see also Sohankar and Davidson (2001)) and it can significantly change the heat transfer and the flow characteristics.

It is worth mentioning that a least square method was employed to fit the results of the present study (Nu, J, f, JF for $\alpha = 20°$) with a power-law function. These correlations are shown in Figs. 6 and 7 and they show good agreement with the calculated results.

In this study a comparison between DNS and LES simulations is performed for $Re = 2000$. It is found that the predicted structures of the flow and temperature field are approximately similar for both methods. This is clearly seen from Fig. 8, where the time-averaged local Nusselt number contours are shown on the bottom wall and the vortex generator. As observed from these figures, the DNS simulation predicts a sharper gradient close to the vortex generators due to use of a finer grid. The agreement between the global results of these simulations is also reasonable. For example, the values of f/J and JF for DNS (*Grid* $162 * 50 * 146$), DNS (*Grid* $122 * 34 * 98$) and LES (*Grid* $122 * 34 * 98$) are $(6.6, 1.78)$, $(6.5, 1.82)$ and $(6.3, 1.90)$, respectively. Thus, from this comparison, similar results (i.e. within 7%) are obtained if one employs a LES simulation with a relatively fine grid instead of a DNS with finer grid. Furthermore, the computational cost for LES is cheaper than DNS. For example, the CPU time per iteration for DNS (*Grid*$162 * 50 * 146$, $Re = 2000$) was about 2.5 times larger than the corresponding value for LES (*Grid* $122 * 34 * 98$, $Re = 2000$) in this study.

Fig. 9 displays the span-wise variation of the normalized turbulence intensities in the x, y and z directions (time-averaged RMS velocity fluctuations, $\sqrt{\overline{u'^2}}, \sqrt{\overline{v'^2}}, \sqrt{\overline{w'^2}}$) at the two positions at the outlet of the computation domain. The first position ($x = 6$, $y = 0.51$) is located in the middle of the channel, while the second one ($x = 6, y = 0.8$) is close to the upper channel wall, see also Fig. 1. There are peak values in the turbulence intensities in the three directions for the first position and they correspond to the core region of the longitudinal vortices, where the strength of the vortices is high. For example at the outlet, the centre of vortices is approximately located at $y \approx 0.4$ and $z \approx \pm 1.25$. The velocity fluctuations are not isotropic and their values exceed 15% in the core region of the vortices. Also, there are high levels of the streamwise intensity close to the lower surface. Such a non-isotropic turbulence intensity is observed throughout the domain, where the longitudinal vortices are active, see Figs. 9 and 10. Fig. 10 shows the time-averaged *RMS* pressure fluctuation, p', *RMS* temperature fluctuation, θ', and turbulent kinetic energy,

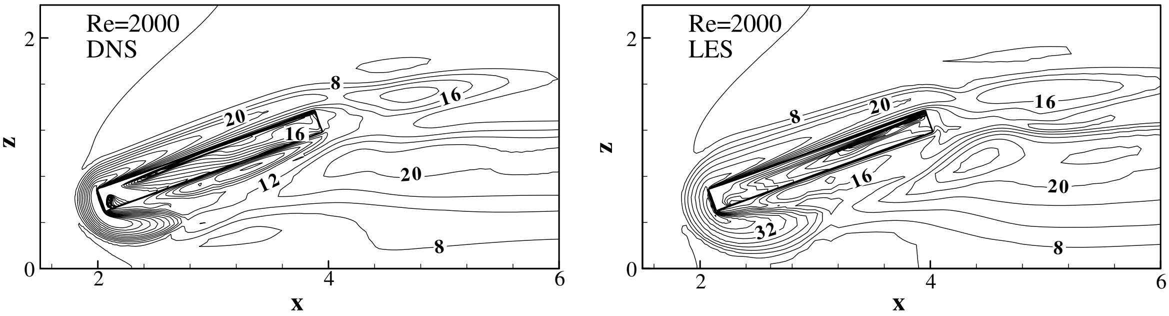

Fig. 8. Time-averaged local Nusselt number contours on the bottom wall and vortex generators, Left: *Grid* $162 * 50 * 146$*DNS*, Right: *Grid* $122 * 34 * 98$*LES*.

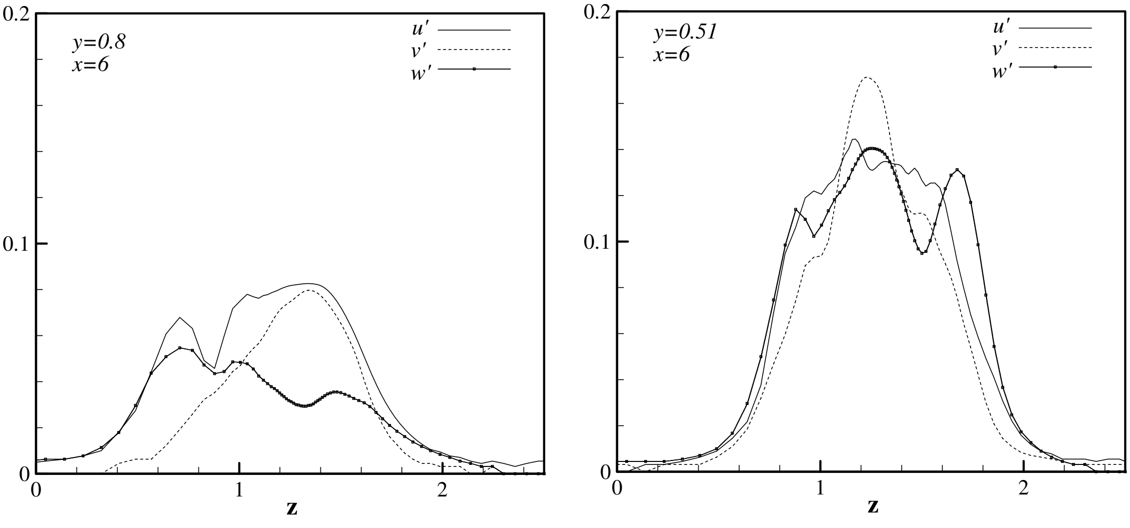

Fig. 9. Variation of time-averaged normalized turbulence intensities (RMS velocity fluctuations) at the two chosen positions, $\alpha = 20°$, $Re = 2000$ DNS.

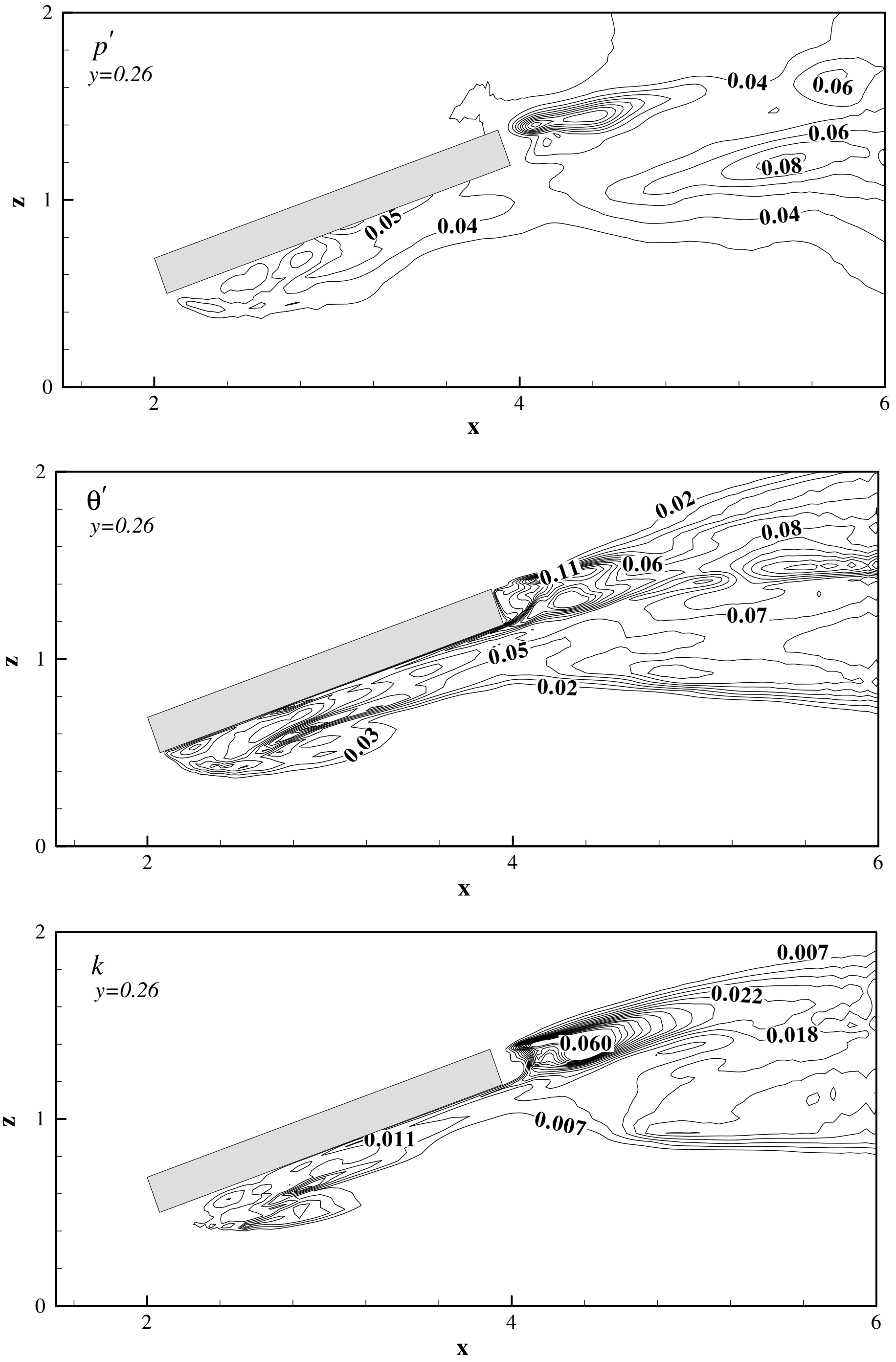

Fig. 10. From top to bottom, time-averaged pressure fluctuations contours, p', temperature fluctuations contours, θ', and turbulent kinetic energy contours, $k = 0.5u'_iu'_i$, $Re = 2000$ DNS, $\alpha = 20°$.

$k = 0.5u'_iu'_i$, on the xz plane at $y = 0.26$. From this figure, it is clear that the levels of the kinetic energy, pressure and temperature fluctuations are higher in the regions where the secondary flow or vortices are more active. It is observed that the turbulent kinetic energy is higher in the vortex core and also near the lower wall. Due to diffusion of the turbulent kinetic energy, it becomes weaker far from the bottom wall and close to the upper wall and also downstream of the vortex generators. It is also seen that the locations of the higher temperature and the pressure fluctuations approximately correspond to those of the higher turbulent kinetic energy, see Fig. 10.

As mentioned above, when the vortex generator is exposed to the main flow, longitudinal vortices are generated. These vortices detach from the vortex generators and form counter-rotating vortex pairs downstream of the vortex generators. In the region where these vortices are active, turbulent flow is generated and there are strong

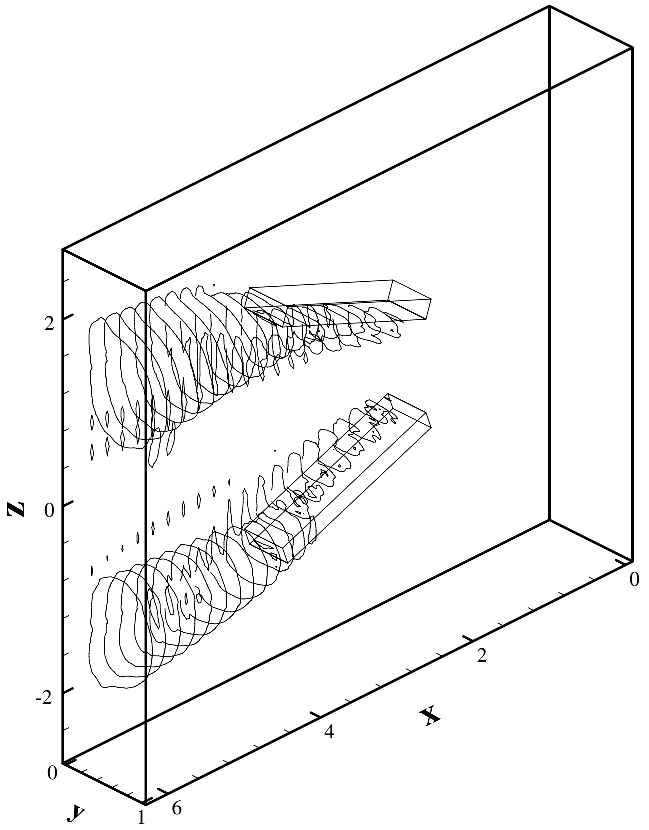

Fig. 11. Three-dimensional structure of time-averaged turbulent kinetic energy, $k = 0.5u'_iu'_i$, $Re = 2000$ DNS, $\alpha = 20°$.

velocity, pressure and temperature fluctuations. This three-dimensional structure of the flow is shown in Fig. 11, where the time-averaged turbulent kinetic energy is plotted. As seen, the shape and the distance between the cores of the longitudinal vortices change as these vortices move downstream of the vortex generators. It is also observed that the cross section of the vortices change from a circular shape close to the vortex generators to an elliptic shape far from the vortex generators. The spaces between the vortex cores in the span-wise direction are 2.2 and 2.5 at $x = 4.5$ and $x = 6$, respectively. In general, the vortex generators largely augment heat transfer with a reasonable pressure penalty in channel flows.

6. Summary and conclusions

The effectiveness of vee-shaped vortex generator is numerically evaluated in a channel typical of those employed in compact heat exchangers. The Reynolds numbers are chosen between 200 and 2000 and for incidence angles ranging from 10° to 30°. It is observed that flow and heat transfer become steady at lower Reynolds numbers while they are unsteady at the higher Reynolds numbers. The present results show that Nusselt number, pressure coefficient, bulk temperature, friction factor and Colburn factor change significantly when the Reynolds numbers and the incidence angles increase. These changes are caused by the generation of the longitudinal and horseshoe vortices with different strengths and circulation. It is found that the vortex strength increases with Reynolds number and it decays in the streamwise direction.

The relation between the key parameters of the velocity (f) and thermal (J) boundary layers of the present results (i.e. $f/J = 5.37 - 7.7$) differs from the predicted value by Chilton–Colburn analogy, i.e. $f/J = 8$. This is because there are some restrictions associated with using Chilton–Colburn relation in all cases.

Thermal performance parameters, $\mathrm{JF} = (J/J^*)/(f/f^*)^{1/3}$, is used as a measure for the amount of heat transfer enhancement relative to the pressure drop. The JF value increases as the Reynolds number increases. The JF value is greater than unity for all selected Reynolds numbers of the present work, when the reference values (J^*,f^*) are employed from the developing channel flow results. A thermal system for the same surface area and pumping power has the better characteristics for heat transfer augmentation, when $\mathrm{JF} > 1$. Thus, the vortex generators largely augment heat transfer with a reasonable pressure penalty.

From a comparison between the DNS and LES results, it is found that if one employs a LES simulation with relatively fine grid instead of a DNS case with finer grid, similar results with cheaper computational cost are obtained. Finally, it is found that the levels of the kinetic energy, pressure, velocity and temperature fluctuations are high in the regions, where the secondary flow or longitudinal vortices are more active, i.e. downstream of and around the vortex generators.

References

Chen, Y., Fiebig, M., Mitra, N.K., 2000. Heat transfer enhancement of finned oval tubes with staggered punched longitudinal vortex generators. International Journal of Heat and Mass Transfer 43, 417–435.

Davidson, L., 1997. Large eddy simulation: a dynamic one-equation subgrid model for three-dimensional re-circulating flow. In: 11th International Symposium on Turbulent Shear Flows, Grenoble, vol. 3, pp. 26.1–26.6.

Davidson, L., 2001. Hybrid LES-RNS: a combination of a one-equation SGS model and a $k - \omega$ model for predicting recirculating flows. In: ECCOMAS CFD Conference, Swansea, UK.

Gentry, M.C., Jacobi, A.M., 2002. Heat transfer enhancement by delta-wing–generated tip vortices in flat plate and developing channel flow. Journal of Heat Transfer ASME 124, 1158–1168.

Germano, M., Piomelli, U., Moin, M., Cabot, W.H., 1991. A dynamic subgrid-scale eddy viscosity model. Physics of Fluids A 3, 1760–1765.

Jacobi, A.M., Shah, R.K., 1995. Heat transfer surface enhancement through the use of longitudinal vortices: a review of recent progress. Experimental Thermal and Fluid Science 11, 295–309.

Jacobi, A.M., Shah, R.K., 1998. Air-side flow and heat transfer in compact heat exchangers: a discussion of enhancement mechanisms. Heat Transfer Engineering 19, 29–41.

Krajnovic, S., Davidson, L., 2002. Large eddy simulation of the flow around a bluff body. AIAA 40 (5), 927–936.

Leu, J.S., Wu, Y.H., Jang, J.Y., 2004. Heat transfer and fluid flow analysis in plate-fin and tube heat exchangers with a pair of block shape vortex generators. International Journal of Heat and Mass Transfer 47, 4327–4338.

Liou, T.M., Chen, C.C., Tsai, T.W., 2000. Heat transfer and fluid flow in a square duct with 12 different shaped vortex generators. Journal of Heat Transfer ASME 122, 237–335.

Mahmood, G.I., Ligrani, P.M., Chen, K., 2003. Variable property and temperature ratio effects on Nusselt numbers in a rectangular channel with 45° angled rib turbulators. Journal of Heat Transfer ASME 125, 769–778.

Schmidt, S., Thiele, F., 2002. Comparison of numerical methods applied to the flow over wall-mounted cubes. International Journal of Heat and Fluid Flow 23, 330–339.

Sohankar, A., 1998. Numerical study of laminar, transitional and turbulent flow past rectangular cylinders, Ph.D. thesis, Department of Thermo and Fluid Dynamics, Chalmers University of Technology, Gothenburg, Sweden.

Sohankar, A., 2004. The LES and DNS simulations of heat transfer and fluid flow in a plate-fin heat exchanger with vortex generators. Iranian Journal of Science & Technology: Transaction B: Technology 28 (B4), 443–452.

Sohankar, A., Davidson, L., Norbeg, C., 1999. A Dynamic one-equation sub-grid model for simulation of flow around a square cylinder. In: 4th International Symposium on Engineering Turbulence Modelling and Measurements, Corsica, France, May 24–26.

Sohankar, A., Davidson, L., Norbeg, C., 2000. Large eddy simulation of flow past a square cylinder: comparison of different subgrid scale models. ASME, Journal of Fluids Engineering 122, 39–47 (see also Erratum, Journal of Fluids Engineering, 122, p. 643).

Sohankar, A., Davidson, A., 2001. Effect of inclined vortex generators on heat transfer enhancement in a three-dimensional channel. Numerical Heat Transfer 39 (Part A), 433–448.

Storey, B.D., Jacobi, A.M., 1999. The effect of stream wise vortices on the frost growth rate in developing laminar channel flows. International Journal of Heat and Mass Transfer 42, 3787–3802.

Webb, R.L., 1994. Principles of Enhanced Heat Transfer. John Wiley & Sons, Chichester, UK.